

COMPUTATIONAL METHODS FOR ANALYZING ELECTRON MULTIPACTING IN RF STRUCTURES

ERKKI SOMERSALO^a, PASI YLÄ-OIJALA^{b,*},
DIETER PROCH^c and JUKKA SARVAS^b

^a *Department of Mathematics, Helsinki University of Technology, Finland;*

^b *Rolf Nevanlinna Institute, University of Helsinki, P.O. Box 4
(Yliopistonkatu 5) FIN-00014, Finland;* ^c *Deutsches Elektronen-Synchrotron
DESY, Hamburg, Germany*

(Received 15 September 1997; In final form 9 January 1998)

Electron multipacting can cause loss of the field level in resonators or it can break the high power rf components like couplers and windows. This phenomenon starts if certain resonant conditions for electron trajectories are fulfilled and if the impacted surface has a secondary yield larger than one. A general cure against multipacting is to avoid the resonant conditions. Therefore, we investigated the dynamics of the electron trajectories in order to find rules for these resonances. We developed new computational methods which combine the standard trajectory calculations with advanced searching and analyzing methods for multipacting resonances. In numerical experiments we consider different coaxial structures. We are able to find those rf incident power levels at which the multipacting occurs and, thereafter, to locate and identify different multipacting processes. We characterize multipacting behavior in straight and tapered lines, and for the straight coaxial line we give simple scaling laws for the multipacting power bands with respect to the diameter, impedance and frequency. Furthermore, the present analysis method turns out to be a powerful tool for optimizing different methods to suppress multipacting. Here, in particular, the biasing DC voltage method is considered.

Keywords: Multipacting; rf structures; Superconducting cavities; Dynamical systems

* Corresponding author. Tel.: +358 9 191 22775. Fax: +358 9 191 22779.
E-mail: Pasi.Yla-Oijala@RNI.Helsinki.FI.

1 INTRODUCTION

Electron multipacting is a major problem in rf structures, especially in superconducting cavities. Multipacting occurs when free electrons, accelerated by the rf field, strike the surface of the cavity and release secondary electrons, which repeat the process and, rapidly cause an electron avalanche. This electron discharge absorbs the rf energy and may cause quenching and breakdown of high power rf components like couplers and windows. The phenomenon starts if certain resonant conditions for electron trajectories are fulfilled and if the impacted surface has a secondary electron yield larger than one.

Basically two different multipacting mechanisms are described in literature.^{1,4,5,9} In the first one, the model case consists of two parallel electrodes with oscillating voltage drop. The resonant electron trajectories bounce from one electrode to another and back in a flight time roughly equal to an integer number of rf cycles. In the second one, the shape of the electron trajectories is mostly due to the magnetic field.

In this article, we describe a systematic computational way to analyze electron multipacting in rf structures. The first step, in the given geometry, is to recognize those rf power levels that are able to multipact. The second step is to locate and identify the possible multipacting processes. The basis of the analysis consists of standard trajectory calculations in relativistic dynamics. The novel feature here is to analyze the general nearly periodic structures of the resonant trajectories by using a special distance function defined in a multidimensional phase space and other ideas arising from the theory of dynamical systems. Preliminary results have been reported previously.^{7,8}

The approach is applied numerically to analyze multipacting in coaxial structures. We consider straight coaxial lines as well as tapered lines and lines with an impedance step. In the straight lines, both the standing wave and traveling wave operations as well as a combination of the standing and traveling wave operations, so-called mixed wave operation, are considered. For the more complicated structures, we have developed our own code for computing the electromagnetic fields. The code is based on the boundary integral equation method for solving Maxwell's equations. A summary of the algorithm is contained in the Appendix.

A general cure against multipacting is to avoid the resonant conditions. Therefore, we investigated the dynamics of the electron trajectories in order to find rules for these resonances and, thereafter, we suppress the multipacting by an appropriate cavity design and field perturbations. For plain coaxial lines, our algorithm enables us to find simple scaling laws for the multipacting power bands with respect to the dimensions, frequency and impedance of the line. By these laws, one can shift the multipacting bands by appropriately altering the design of the line. Furthermore, we studied the effect of grooving to multipacting as well as DC biasing and static magnetic perturbations of the rf field. With our present multipacting analysis method, it is possible to optimize the perturbations and suppress the multipacting to acceptably low levels.

2 MULTIPACTING AND DYNAMICS

Physically, the multipacting process is described as follows. An electron is emitted from the surface of an rf cavity and driven by the field. When it impacts the cavity wall, it may release one or more electrons from the surface of the wall, the number of the secondary electrons depending on the impact energy and the wall material characteristics. These secondary electrons are again accelerated by the field, yielding new impacts and possibly new secondary electrons. In appropriate conditions, the number of electrons may increase exponentially, leading to remarkable power losses, gassing of the surface and heating of the walls.

One illustrating model case of multipacting consists of two parallel electrodes with an oscillating voltage drop. Denote the distance of the electrodes by $d > 0$, and assume that the voltage between the electrodes is given by the formula

$$U(\varphi) = U_0 \sin \varphi, \quad (1)$$

where $0 \leq \varphi < 2\pi$ is the phase of the field. Denote the rf frequency of the field by f . Using non-relativistic dynamics, an electron leaving the electrode with lower voltage at the initial phase φ_0 and zero initial velocity is at the distance

$$x(t) = \frac{\alpha U_0}{d(2\pi f)^2} ((\varphi - \varphi_0 + 2\pi n) \cos \varphi_0 - (\sin \varphi - \sin \varphi_0)) \quad (2)$$

from the electrode at a later time $t = (\varphi/2\pi + n)/f$, or $\varphi = \varphi(t) = 2\pi(tf - n)$. Here, $\alpha (= e/m) > 0$ is the charge-to-mass ratio of the electron. By requiring that the electron leaving at the initial time t_0 and phase φ_0 , hits the other electrode at $t = t_0 + (n - 1/2)/f$, $n = 1, 2, \dots$, i.e., $\varphi = \varphi_0 + (2n - 1)\pi$ and $x(t_0 + (n - 1/2)/f) = d$, we get the following resonant condition for the peak voltage:

$$U = U_n(\varphi_0) = \frac{(2\pi df)^2}{\alpha} \frac{1}{2\pi(n - 1/2) \cos \varphi_0 + 2 \sin \varphi_0}, \quad n = 1, 2, \dots \quad (3)$$

for the two-point multipacting between the electrodes. Note that after n full rf cycles, the trajectories of the possible secondary electrons emitted from the opposite electrode hit the first electrode. In the particular case $\varphi_0 = 0$, we get the following well-known formula:

$$U = U_n = \frac{4\pi(df)^2}{\alpha(2n - 1)}, \quad n = 1, 2, \dots \quad (4)$$

Formula (4) gives the theoretical upper limit for the resonance voltage and the lower limit is obtained from (3) by letting φ_0 vary from 0 to π .

Generalizing the reasoning to arbitrary rf cavities, the resonance conditions for multipacting can be written as follows:

- (1) An electron emitted from the cavity wall is driven by the EM fields and returns back after an integer number of rf cycles to the same point of the cavity wall;
- (2) The impacting electron produces more than one secondary electron.

If conditions (1) and (2) are fulfilled and if there have been m impacts and n full rf cycles before the electron returns back to the emission point, the process is called as an $(m + 1)$ point n th order multipacting process.

In the case of the traveling wave in structures like straight waveguides and coaxial lines the above condition (1) should be modified as follows. The emitted electron, after an integer number of rf cycles, returns and impacts the wall at a moment of time when the field conditions are the same at the location of the impact as they were at the

location of emission, and, accordingly, the trajectory will be repeated by the possible secondary electrons.

By using this simple geometry as a model case, we formalize the above ideas to general cavities in terms of dynamical systems.

2.1 The Dynamical System

In the sequel, we assume that the electron dynamics is governed by relativistic dynamics. Assuming that the effect of the field of the electron itself on the external field is negligible, the dynamics of a relativistic electron in an electromagnetic field, is generated by the equations

$$\begin{cases} \frac{d\mathbf{v}}{dt} = -\alpha \left(1 - \left(\frac{v}{c}\right)^2\right)^{1/2} \left(\mathbf{E} + \mathbf{v} \times \mathbf{B} - \frac{1}{c^2}(\mathbf{v} \cdot \mathbf{E})\mathbf{v}\right), \\ \frac{d\mathbf{x}}{dt} = \mathbf{v}, \end{cases} \quad (5)$$

where \mathbf{v} is the 3-velocity of the electron, $v = |\mathbf{v}|$, and c is the speed of light in vacuum.²

Let Ω be a void cavity with a time harmonic electromagnetic field,

$$\mathbf{E}(x, \varphi) = \mathbf{E}(x) \sin \varphi, \quad \mathbf{B}(x, \varphi) = \mathbf{B}(x) \cos \varphi. \quad (6)$$

Here, for convenience, the phase $\varphi = \varphi(t) = 2\pi t/T$ plays also the role of the normalized time with $T = 1/f$.

Denote the wall of Ω by $\partial\Omega$, and assume that the field map is known. Consider an electron being emitted at a point x_0 of the cavity wall $\partial\Omega$, the field phase at the time of emission being φ_0 , $0 \leq \varphi_0 < 2\pi$. Furthermore, it is assumed here that the initial velocity v_0 of each electron is normal to the cavity wall and of constant size, typically a few eV. This assumption is a representative average of the real physical initial conditions of the emitted electron population, and it leads to an adequate modelling of the multipacting trajectories. Suppose that the electron is driven by the EM fields according to the system (5). Denote by x_1 the point and by φ_1 the field phase, where the electron hits the cavity wall for the first time. We may define a mapping

$$R : (x_0, \varphi_0) \mapsto (x_1, \varphi_1). \quad (7)$$

Using the notation $X = \partial\Omega \times [0, 2\pi]$, the above mapping R defines a dynamical system in the *phase space* X : Each point $p = (x, \varphi) \in X$ generates a discrete trajectory $\{p, R(p), R^2(p), \dots\}$.

Let us divide the phase space X into an electron emitting and non-emitting part by writing $X = G \cup W$, where

$$G = \{(x, \varphi) \in X \mid \mathbf{n}(x) \cdot \mathbf{E}(x, \varphi) \leq 0\}, \quad (8)$$

$$W = \{(x, \varphi) \in X \mid \mathbf{n}(x) \cdot \mathbf{E}(x, \varphi) > 0\} = X \setminus G. \quad (9)$$

Here, $\mathbf{n}(x)$ is the unit normal vector at $x \in \partial\Omega$ pointing into the cavity. In other words, W consists of those points of the phase space where a free electron is immediately captured to the wall by the field while the electrons leaving G are injected into the cavity by the electric field. We assume here that the initial kinetic energy is negligible. The set G is called the *bright set*, while W is called the *shadow set*.

We can now rewrite the first condition (1) in the terms of R mapping by

$$R^n(p) = \underbrace{R \circ R \circ \dots \circ R}_{n \text{ times}}(p) = p, \quad p \in G, \quad (10)$$

i.e., $p \in G$ is a fixed point of the iterated mapping R^n . For the secondary yield we define another function. Let $E_{\text{kin}}(p)$ be the kinetic impact energy of the electron starting at p and denote the secondary electron yield function of the cavity wall by δ . This function depends on the impact energy and the properties of the material at the location of the impact, i.e., $\delta = \delta(x, E_{\text{kin}})$. A typical curve $E_{\text{kin}} \mapsto \delta(x, E_{\text{kin}})$ obtained from the literature⁵ is displayed in Figure 1 (the one we have used in our calculations).

We define the *multiplicity function* α as

$$\alpha : X \rightarrow \mathbb{R}, \quad \alpha(p) = \delta(x_1, E_{\text{kin}}(p)), \quad \text{where } R(p) = (x_1, \varphi_1). \quad (11)$$

Thus, the function α simply tells how many secondary electrons (in average) each initial electron in the phase space will produce when impacting the wall. Note that in the shadow set we define naturally

$$\alpha(p) = 0, \quad p \in W. \quad (12)$$

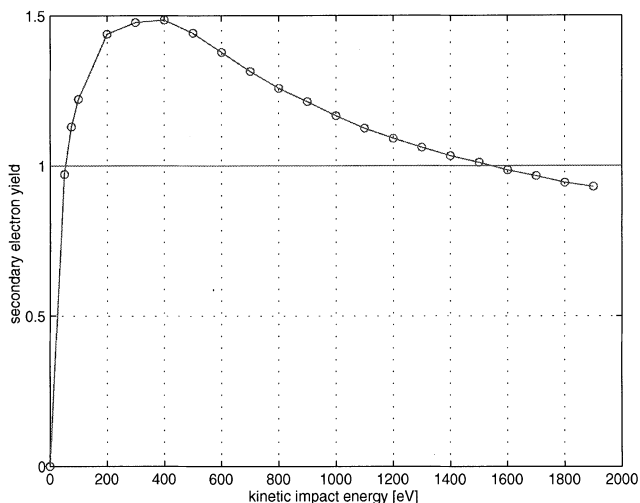


FIGURE 1 The secondary electron yield at different impact energies (in eV) for a niobium surface baked at 300°C.

Considering the full discrete trajectory, the number of secondary electrons due to one single electron starting at p after n impacts is

$$\alpha_n(p) = \prod_{j=0}^{n-1} \alpha(R^j(p)), \quad p \in G. \quad (13)$$

Now the second condition (2) for multipacting can be written in the terms of the multiplicity function by

$$\alpha_n(p) > 1, \quad p \in G. \quad (14)$$

2.2 Counter and Distance Functions

Our aim is to develop methods by which we can, on one hand, find those EM field levels at which the electron multipacting may occur, and, on another hand, analyze the mechanism of the process at the found multipacting field levels. Especially, we want to find the location of the multipacting process in the phase space, and also, to compute the multipacting trajectories and find their kind (one-point, two-point, etc.) and order.

Let us first look at the problem of finding possible multipacting power levels. Let us assume that we are interested in a power interval $[P_{\min}, P_{\max}]$. We choose a representative sample of power values from this interval and for each fixed power value we do the multipacting analysis along the following lines. First, we pick a large number of initial points p_j in the phase space X and for each point p_j compute the discrete trajectory $\{p_j, R(p_j), R^2(p_j), \dots\}$. After a fixed number n of iterations of the map R , we count those electron trajectories that were still in the bright set, and hence able to multipact. This count is denoted by $c_n = c_n(P)$,

$$c_n(P) = \#\{p_j \mid R^n(p_j) \in G\}, \quad (15)$$

i.e., c_n is the number of surviving trajectories after n impacts. Obviously, if c_n is large for a large n , the geometry favors trajectories that may cause multipacting. Since no information of the secondary electron yield is included in c_n , a large value does not necessarily mean that multipacting occurs.

In order to take the secondary yield into account, we define an *enhanced counter function* as a sum of multiplicity functions of single electrons after n iterations

$$e_n(P) = \sum_{j=1}^L \alpha_n(p_j), \quad (16)$$

where L is the number of initial electrons and $\alpha_n(p_j)$ gives the secondary yield due to j th electron after n impacts. The enhanced counter function is a good indicator for strong multiplication, i.e., whether the secondary yield is large enough for multipacting.

The functions c_n and e_n provide means of recognizing possible multipacting powers. Once the multipacting levels are recognized, we need to locate the processes in the phase space. Especially, we are interested in finding those points that satisfy the fixed point condition (10), or more generally points p with $p - R^n(p)$ small in an appropriate sense. An effective way of searching for those points p in the phase space is to consider the *distance function*

$$d_n(p) = \sqrt{|x_0 - x_n|^2 + \gamma |e^{i\varphi_0} - e^{i\varphi_n}|^2}, \quad (17)$$

where $p = (x_0, \varphi_0)$ and $(x_n, \varphi_n) = R^n(p)$. Here, γ is a scaling constant, e.g., chosen so that one discretization step in the phase direction affect d_n roughly as much as one in the distance direction. The distance function d_n tells how far away the trajectory is after n impacts from the initial point. The minima of d_n give the initial points of those trajectories that correspond to multipacting. Note that the minimum search must be restricted to the area where $\alpha_n(p) > 1$.

A recomputation of the trajectories starting at the minima of d_n can be used to analyze the nature of the multipacting process. The important questions are the order of the multipacting, whether it is a one-point or multi-point multipacting and whether it is mostly due to the magnetic or electric field.

3 NUMERICAL EXPERIMENTS

In this section we apply the ideas to different geometries. First, the algorithm is verified by using the two-electrode model as a test problem. This is a simple model for multipacting in rectangular waveguides.¹¹ Other geometries are different coaxial structures.

3.1 Model Problem: Parallel Electrodes

Consider the non-relativistic electrons between two parallel electrodes with an oscillating voltage drop described in the previous section. In terms of the peak voltage, the resonant multipacting levels are obtained from formula (3). The first test is to see how well these values correspond to the local maxima of the counters $c_n(U)$ and $e_n(U)$. In Figure 2, we have plotted the counter function c_n computed by using 180 initial electrons with different initial phases. The theoretical upper and lower limits for the resonance voltages U_n given in (3) are marked in the figure. For the first order process corresponding to the highest voltage, for example, the upper and lower limits are obtained from (3) by substituting $\varphi_0 = 0$ and $\varphi_0 = 32$ degrees, respectively. Figure 2 shows that multipacting may occur in a relatively broad voltage band. Typically, lower order multipacting bands are broader than the higher order bands, the bandwidth decreasing roughly inversely proportionally to $(1+n)^4$, where n is the order of the process. This phenomenon is

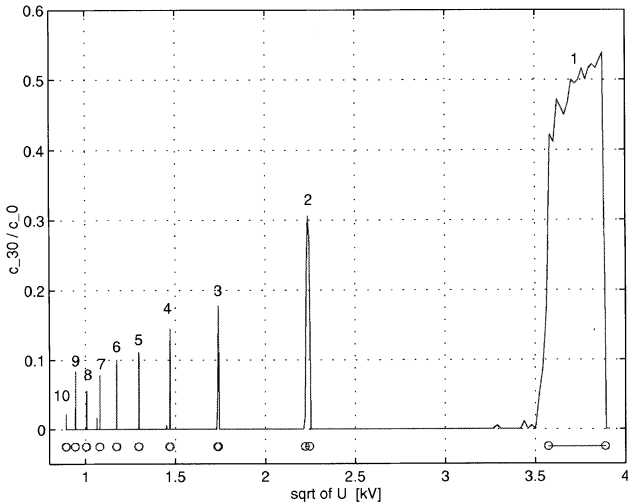


FIGURE 2 Relative counter ($c_{30}(U)/c_0(U)$) after 30 impacts. The abscissa is $U^{1/2}$ and the voltage U is given in kV. The 10 first theoretical values U_n (upper and lower limits) are marked by circles. The first order process is on the right, then the second order process, etc., i.e., the order increases when moving to the left. The distance of the electrodes is 29.1 mm and the frequency is 500 MHz.

encountered in actual multipacting experiments, too.⁶ It should be emphasized that this broadening is not due to varying initial velocities of the emitted electrons: In our calculations, the initial velocities are kept fixed. Rather, the bandwidth should be understood as measure of the stability of the multipacting process with respect to the perturbations of the field. This phenomenon is clearly demonstrated in Figure 3, where we have plotted the distance function (defined in (17)) due to the first order process. The process is found to be strongly phase focusing, i.e., the electrons cluster to certain phase values. In Figure 3, the darkest band is the attracting phase and the shaded areas around it are the focused phases. Theoretical resonance voltage/initial phase values are marked in the figure. However, only the lower part of the theoretical curve is focusing, the upper part turns out to be defocusing.

Next the effect of the secondary electron yield to the counter function is checked. First, Figure 4 shows the average impact energy of those electrons which are still in the bright set after 30 impacts. Between the solid lines the secondary yield corresponding to the curve in Figure 1 is greater than one, and the maximum yield 1.5 is reached when the

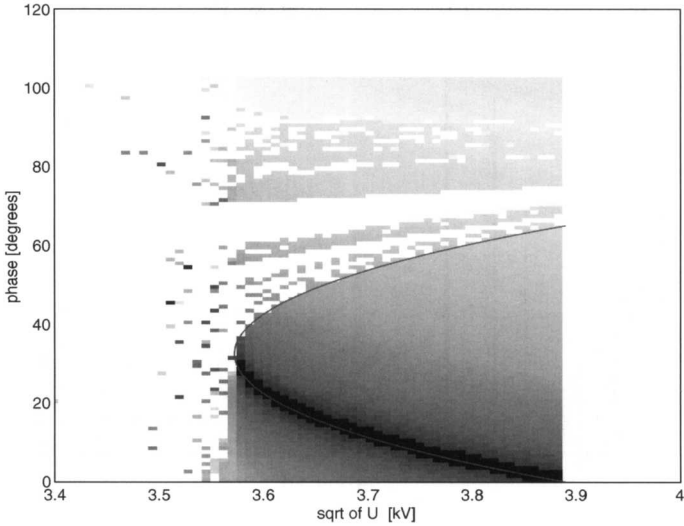


FIGURE 3 Distance function due to the first order process. The vertical axis gives the initial phase in degrees and the horizontal axis is $U^{1/2}$ in kV. Theoretical resonance voltage/initial phase values are marked by a curve.

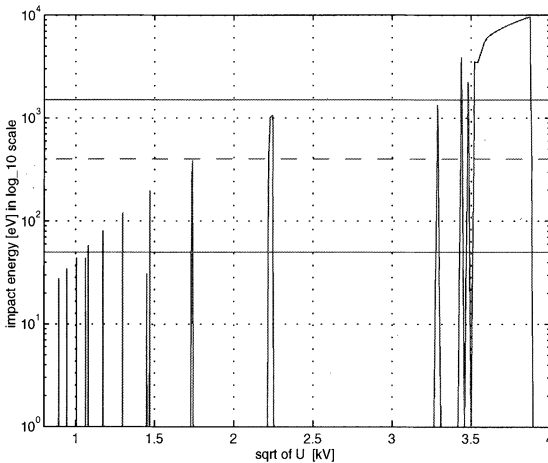


FIGURE 4 The average impact energy in eV. The vertical axis gives the impact energy in 10 base logarithmic scale. Between the solid lines the used secondary yield is greater than one, i.e., when $50 \text{ eV} \leq E_{\text{kin}} \leq 1500 \text{ eV}$, and along the dashed line ($E_{\text{kin}} = 400 \text{ eV}$) the maximum yield 1.5 is reached. The third order process seems to have optimal impact energy for multipacting. This is shown in Figure 5, where the third order process have the highest peak, i.e., the greatest number of secondary electrons.

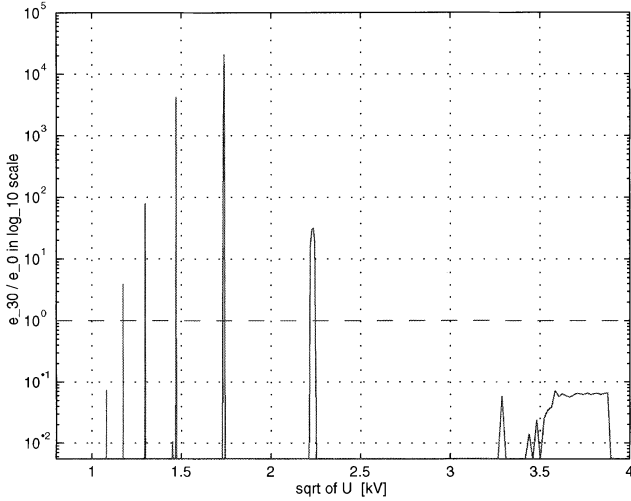


FIGURE 5 Relative enhanced counter function in the logarithmic (base 10) scale after 30 impacts. Note that multipacting occurs only when the relative enhanced function (in the logarithmic scale) is greater than one, i.e., the number of the electrons is increased.

impact energy is close to the dashed line. Figure 4 suggests that only processes of order 2–6 correspond to multipacting processes. For the lowest order process, the kinetic impact energy is too high to produce secondaries while for the processes of order 7 and up the kinetic energy is too low. This is clearly demonstrated in Figure 5, where we have plotted the enhanced electron counter functions e_n .

3.2 Coaxial Lines: Standing Wave

Here we apply the multipacting analysis to straight coaxial lines in standing wave (SW) operation.

Let a and b denote the inner and outer radii of the coaxial line. If f is the frequency and U is the voltage drop between the inner and outer conductor, the TEM-mode fields in SW operation are given by the formulae

$$\begin{aligned}
 E_{\text{SW}}(x, \varphi) &= \frac{U}{2r \ln(b/a)} (\cos(kz - \varphi) - \cos(kz + \varphi)) \mathbf{e}_r, \\
 B_{\text{SW}}(x, \varphi) &= \frac{U}{2cr \ln(b/a)} (\cos(kz - \varphi) + \cos(kz + \varphi)) \mathbf{e}_\theta.
 \end{aligned}
 \tag{18}$$

Here $k = \omega/c = 2\pi/\lambda$ and (r, θ, z) is the representation of the field point x in cylindrical coordinates. The average *incident power* flow P of the electromagnetic field is related to the voltage U through the formula

$$P = \frac{U^2}{8Z}, \quad Z = \frac{\eta_0}{2\pi} \ln \frac{b}{a}, \quad (19)$$

where Z is the line impedance and $\eta_0 = \sqrt{\mu_0/\epsilon_0}$ is the wave impedance in vacuum.

By the symmetry of the standing wave fields, we restrict the computations to a segment of the line of length one quarter of the wavelength, from the maximum to the first zero of the electric field.

By the form of the rf fields, it is obvious that electrons with the initial velocity in a plane $\theta = \text{constant}$ remain in that plane. To find the possible multipacting power bands, we compute the counter function $c_n(P)$. Figure 6 shows the plot of the function $c_n(P)$. Here, initial electrons are sent both from the inner and outer conductor. By considering the distance functions it is found that the surviving trajectories appear near the maximum of the electric fields. To verify this conclusion, we compute separately the counter functions for electrons initiated at the electric field maximum only, and on the other hand for electrons starting from the maximum to the first zero of the electric field. These functions are plotted in Figure 6. Evidently, the major features of the counter function in the top frame of Figure 6 are repeated in the bottom frame. Essential contribution from electrons outside the electric field maximum comes only at high incident powers. We may deduce that at least within the incident power range used in our calculations, multipacting in coaxial lines with a standing wave is predominantly due to the electric field only. In fact, electron trajectories perturbed off the maximum of the electric field are bending towards the minimum due to the magnetic field. Hence, the electrons are drifting towards the shadow set. A further analysis of the dynamics shows that the multipacting processes are strongly phase-focusing, i.e., all the electrons near the electric maximum are clustered to well defined phase values. Thus, *there are points in the phase space that are repelling in the spatial direction but attractive in the phase direction*. This phenomenon is demonstrated clearly in Figure 7, where we have plotted the locations of 1000 electrons on the outer conductor after 1, 2 and 4 impacts when the incident

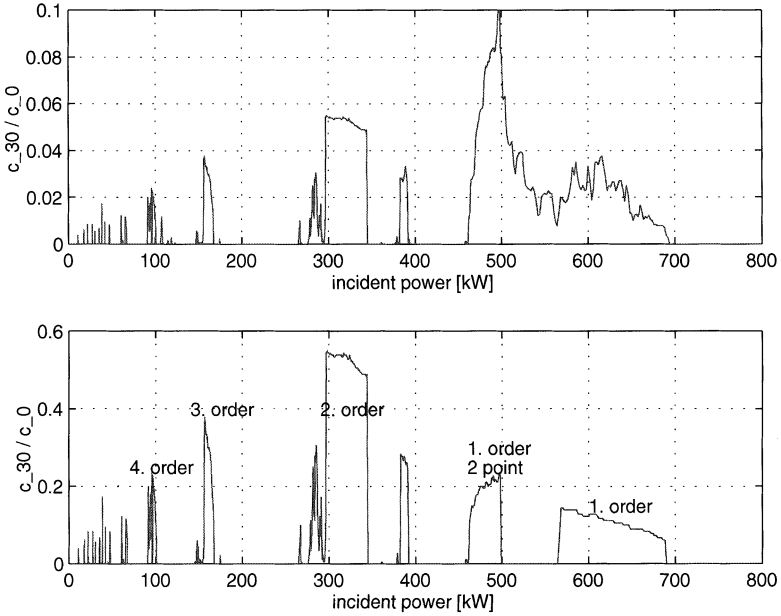


FIGURE 6 Relative electron counter functions after 30 impacts. The computation was done with a $50\ \Omega$ line with inner and outer radii $a=22.4\text{ mm}$, $b=51.5\text{ mm}$, respectively, at the frequency 500 MHz . In the top frame, electrons from $\lambda/4$ (maximum electric field) to $\lambda/2$ (maximum magnetic field) were tracked, and in the bottom frame, the initial electrons were restricted to the maximum of the electric field only. The differences showing in these plots (from 450 to 690 kW) are due to the first order two-point process. Note the different scaling of the figures.

rf power is chosen from one of the multipacting bands. A further demonstration of the phase focusing is seen in Figure 8, where we have plotted the distance $|\varphi - \varphi_n|$, i.e., the difference between the original and final phases after n impacts for each incident power. Here, the electron trajectories are initiated only at the maximum of the electric field. The darkest areas are the attracting phases, and the shaded areas around them are the focused phases.

Basically two different dominant multipacting types can be recognized. First, there are one-point multipacting processes of different order on the outer conductor of the line. Secondly, there are two-point processes from the outer conductor to the inner one and back. In addition, we were able to find some more complicated processes that show up only on relatively narrow power bands that are usually overlapping with the more prominent one- and two-point bands. An

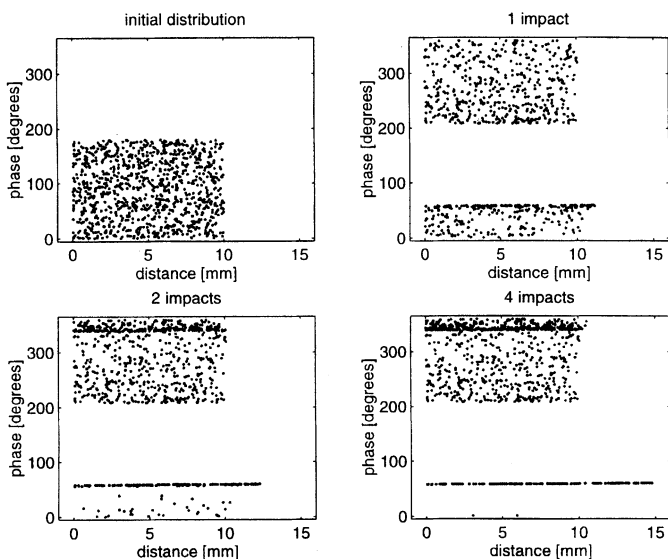


FIGURE 7 The initial electron distribution and the distributions after 1, 2 and 4 impacts corresponding to a first order one-point process. Horizontal axis gives the distance from the electric field maximum in millimeter and the vertical axis gives the phase of the field in degrees. Here, the electrons only on the outer conductor are plotted. Phases from 0 to 180 correspond to the bright set and phases from 180 to 360 correspond to the shadow set. All electrons in the bright set cluster to a certain phase value (close to 60°) after a few impacts.

exceptionally prominent peak corresponding to the more complicated trajectories appear around 390 kW. The process is a combination of a two-point process of order one and a one-point process of order two.

The order and the type of the most prominent process in each power band is indicated in Figure 6. The merging of the two different first order processes is due to electrons with relatively stable trajectories outside the maximum of the electric field. An analysis of the trajectories shows that these electrons are order one two-point multipactors.

For comparison, Figure 9 shows the enhanced electron counter versus incident power plotted in the logarithmic (base 10) scale. The analysis was restricted here to the maximum of the electric field. The peaks with values greater than one represent power levels when multipacting is probable. Note again that at high rf powers, the kinetic energy is prohibitively high for secondary electrons to appear.

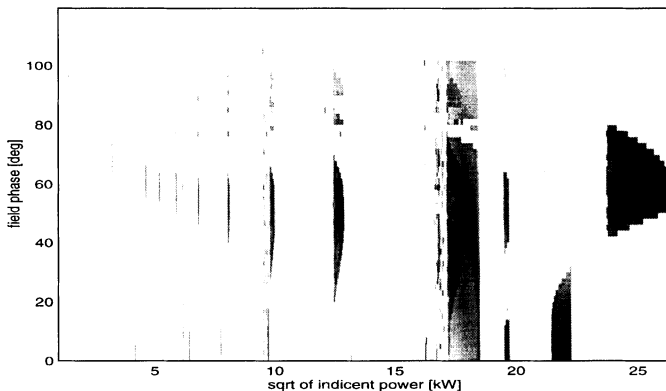


FIGURE 8 The gray scale contour plot of the distance function d_{30} when the primary electron emission is restricted to the maximum of the electric field. The darkest shading corresponds to the minima. Initial phases corresponding to electron trajectories that end up to the shadow are marked with white. Same geometry as in Figure 6. The horizontal axis gives the square root of the incident power in kW and the vertical axis gives the field phase in degrees.

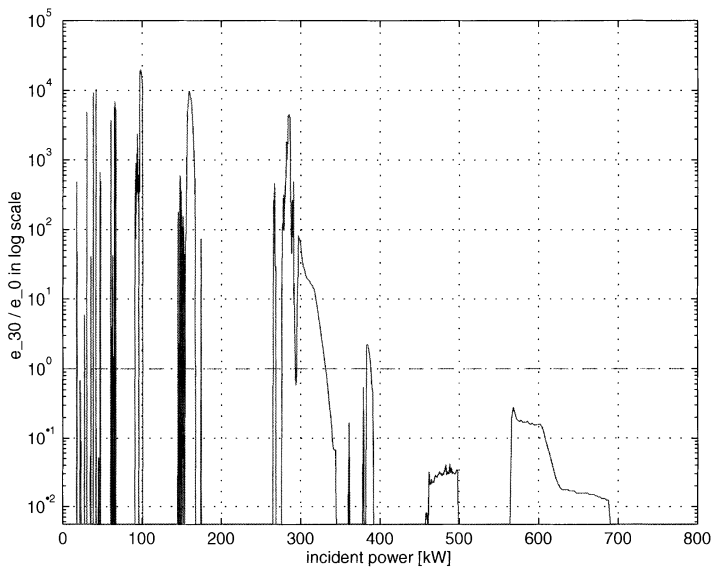


FIGURE 9 Relative enhanced counter function in the logarithmic (base 10) scale restricted to E_{\max} , same geometry as in Figure 6. Note that when multipacting occurs, the relative enhanced function (in the logarithmic scale) is greater than one, i.e., the number of the electrons is increased.

Next, we examine the question whether the multipacting phenomena described above obey some simple scaling laws. More specifically, we perform the multipacting analysis with coaxial lines with different dimensions as well as with different rf frequencies, and identify in each case the multipacting processes of different type and order. The idea is to find simple rules relating multipacting power levels and geometric parameters.

The first natural question is what the ratios of the field intensities are corresponding to the same multipacting process of different order. In Figure 10, the maxima of the electric field at the outer conductor are plotted versus the inverse of $(n + 1)$ where n is the order of one-point multipacting, yielding an approximately linear dependence. This suggests that the multipacting field values are proportional to $1/(n + 1)$.

Next, we check the effect of varying the frequency f of the field. By computing data sets equivalent to Figures 6 and 9 with different frequencies, the general form of the counter functions remains strikingly

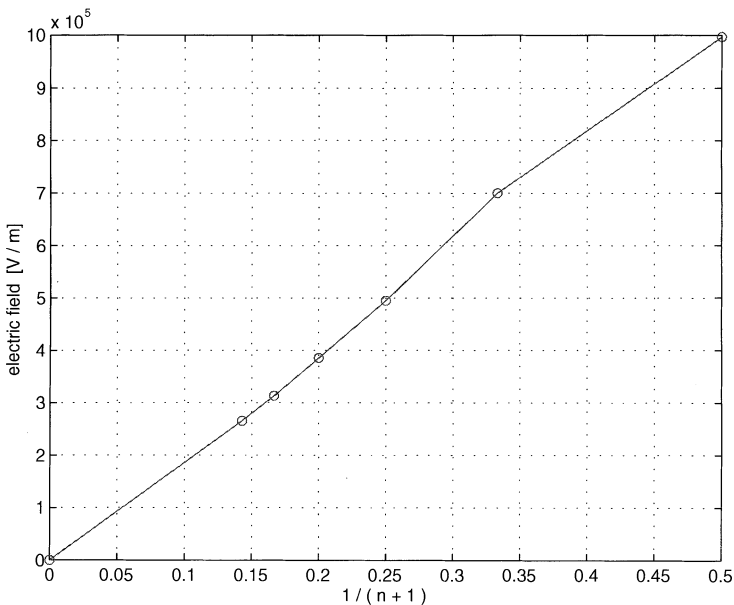


FIGURE 10 The peak values of the electric field at the outer shell of the coaxial line. The horizontal axis is $1/(n + 1)$, where n is the order of the multipacting. The outer diameter of the line is 40 mm, impedance is 50 and the frequency is 1.3 GHz.

similar and it is easy to identify corresponding processes and recognize the power levels of the multipacting processes of different type and order. In Figure 11(a), we have plotted the rf frequency versus the square root of the peak values of the electric field when the line multipacts. The multipacting processes here are one-point multipacting, the order being indicated in the plot.

The effect of geometric dimensions of the coaxial line is studied in the similar fashion. Let both the inner and outer diameter of the line vary so that the impedance of the line remains unaltered, i.e., $b/a = \text{constant}$. Again, the counter function plots retain their shape, and similarly to the previous case, we may locate the one-point multipacting rf powers of different order. Figure 11(b) depicts the peak values of the electric field at multipacting powers.

The results of Figures 10 and 11 can be summarized in a concise way as a scaling law: The one-point multipacting powers in a coaxial line with fixed impedance obey the rule

$$P_{\text{one-point}} \sim \frac{d^4 f^4}{(n+1)^2}, \quad (20)$$

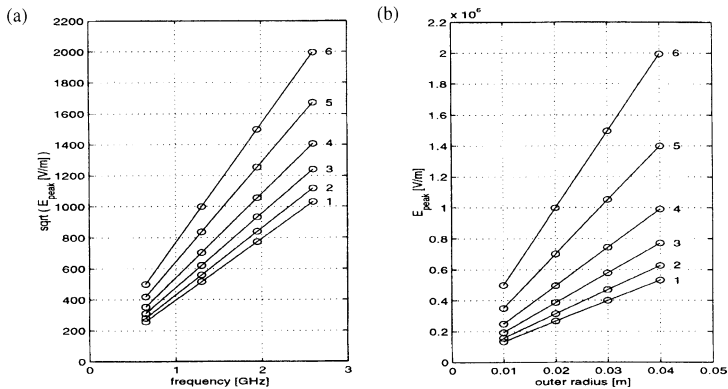


FIGURE 11 (a) The curves represent the effect of varying the rf frequency. In the experiment, the radial dimensions of the coaxial line were kept fixed. The outer radius is 20 mm and the impedance is 50. The labels indicate the order of the multipacting, and the curve indicates the square root of the peak value of the electric field at the outer shell at which the multipacting occurs. (b) The rf frequency is fixed at 1.3 GHz and the radial dimensions of the coaxial line are changed, keeping the impedance of the line fixed ($= 50$), i.e., the ratio of the inner and outer radius is unaltered. The horizontal axis is the radius of the outer shell, the vertical one the maximum of the electric field at the outer radius.

where f is the frequency of the field, d is the outer diameter of the line and n is the order of the process. This scaling law with respect to the frequency and dimensions agrees with the experimental ones found by Woo.¹⁰

We were able to find a similar dependence on frequency and dimension for two-point multipacting process. The dependence on the order is harder to verify since the two-point processes of order higher than one appear at powers overlapping with predominant one-point processes and consequently, the identification is more difficult.

So far, the impedance of the line was fixed. To find a scaling law for impedance we made the following numerical experiment: The rf frequency and the diameter of the outer conductor were fixed, while the inner diameter was varying, corresponding to a varying impedance, obtained from formula (19). For each line impedance the multipacting levels were computed and identified. The multipacting analysis was restricted to the maximum of the electric field. With different impedances, the counter functions do not have a shape as invariant as with respect to frequency and dimension perturbation. However, the different processes can be identified. In Figure 12, we have plotted the bounds of each multipacting band with different line impedances. Multipacting processes identified to belong to the same family are joined with lines and the order of each process is indicated in the plot. The one-point processes are marked with a circle and the two-point process of order one with an asterisk. The conclusion is that the one-point multipacting levels depend approximately linearly on the line impedance, while the two-point multipacting levels depend quadratically on it. The coefficient of this dependence is a function of the order of the process. Combined with the previously obtained results, we may thus write a scaling law for the impedances as

$$P_{\text{one-point}} \sim (fd)^4 Z, \quad P_{\text{two-point}} \sim (fd)^4 Z^2. \quad (21)$$

To get the complete picture, the secondary electron yield must be included. Therefore, we compute the average kinetic impact energies of the multipacting electrons for each process. It is found that with a fixed impedance, the average impact energy obeys roughly the scaling law

$$E_{\text{kin}} \sim (fd)^2, \quad (22)$$

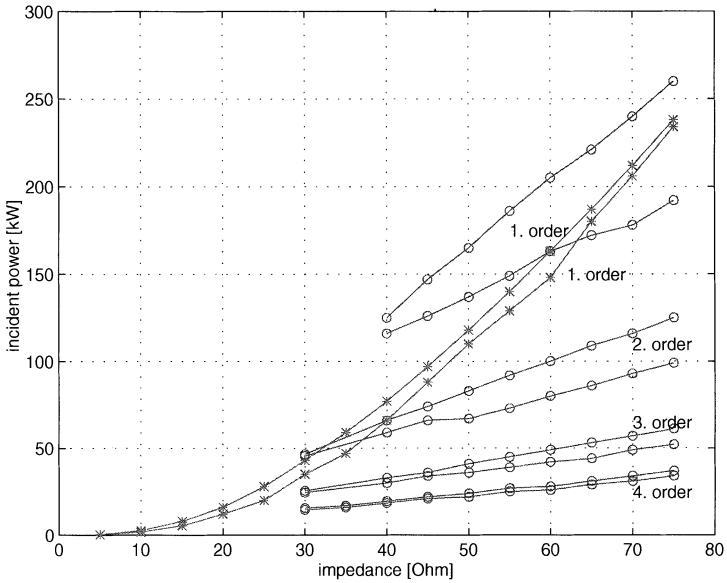


FIGURE 12 The bounds of each multipacting band with different line impedances for 352 MHz, 50 Ω coaxial line with inner and outer radius $a=22.5$ mm and $a=51.5$ mm, respectively. The impedance is changed by varying a while b is fixed. Multipacting processes identified to belong to the same family are joined with dashed lines and the order of each process is indicated in the plot. The one-point processes are marked with a circle and the two-point process with an asterisk. The computation for the one-point processes is stopped at 30 Ω (40 Ω for the first order process) because the multipacting bands get narrower and harder to identify at lower impedances.

in accordance to a simple dimension analysis. Typically the secondary electron yield for niobium is larger than one in the range ~ 100 –1500 eV (see Figure 1). Figure 13 is a graphical summary of the multipacting analysis in coaxial lines including the scaling laws and the secondary yield.

3.3 Traveling Wave and Mixed Operation

It is important to understand the behavior of multipacting when the field is switched from standing wave to the traveling wave (TW), i.e., the reflected wave vanishes. It turns out that the distribution of the multipacting levels of purely one-way traveling wave resembles the standing wave case. However, for partly reflected waves, the situation is more complicated.

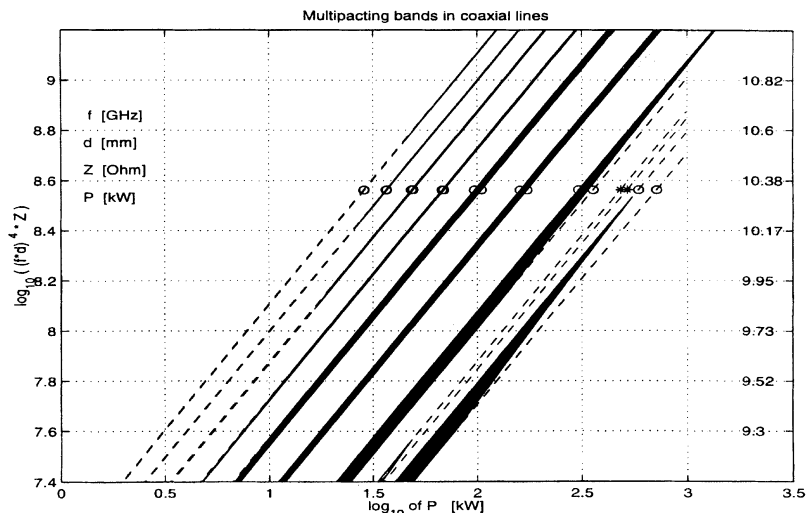


FIGURE 13 The graphical summary of the multipacting analysis in coaxial lines including the scaling laws and the secondary yield. The left vertical axis is for one-point multipacting processes, the processes marked by circles, in the base 10 logarithm of $(fd)^4 Z$ (in $(\text{GHz} \times \text{mm})^4 \times \Omega$), and the right vertical axis is for two-point processes, the processes marked by asterisks, in the base 10 logarithm of $(fd)^4 Z^2$ (in $(\text{GHz} \times \text{mm})^4 \times \Omega^2$). The horizontal axis is the base 10 logarithm of the incident power (for all processes, in kW). The lowest band (at right) is the first order one-point multipacting band. The next band upwards is a two-point first order band, then follows a set of one-point bands, the order increasing up to 8 when the figure one moves up to lower powers (to left). The circles (one-point) and asterisks (two-point) in the picture correspond to the 50Ω , 1.3 GHz , 40 mm (outer diameter) line. The dark parts of the bands represent the areas when multipacting may occur, i.e., the average impact energy is in the range $\sim 100\text{--}1500 \text{ eV}$ and the secondary yield is larger than one.

Let us start with the pure TW wave. The TEM-mode fields in TW operation are given by the formulae

$$\begin{aligned} E_{\text{TW}}(x, \varphi) &= \frac{U}{2r \ln(b/a)} (\cos(kz - \varphi)) \mathbf{e}_r, \\ B_{\text{TW}}(x, \varphi) &= \frac{U}{2cr \ln(b/a)} (\cos(kz - \varphi)) \mathbf{e}_\theta, \end{aligned} \quad (23)$$

with $c = (\varepsilon_0 \mu_0)^{-1/2}$.

The computation of the counter function c_n with no reflected wave has a very similar shape as in the case of complete reflection.¹²

A closer analysis of the multipacting trajectories show that there is a simple scaling rule between the multipacting levels of different order in the traveling and standing wave operations, given by the formula

$$P_{\text{TW}} = 4P_{\text{SW}}, \quad (24)$$

i.e., in the traveling wave operation the multipacting processes remain the same but they appear at rf power levels four times higher than in the SW case. Heuristically, one could give a simple physical explanation to this phenomenon: the peak voltage in the standing wave operation is twice the peak voltage of the traveling wave. The analysis of the trajectories show, however, that the situation is more subtle, since the multipacting electrons are traveling along with the wave as the wave form moves. Thus, the magnetic field must play a crucial role in the process. The wall impacts of the stable trajectories appear close to the maximum of the electric field. This traveling of the multipacting locations is quite slow; in the $50\ \Omega$ line with 1.3 GHz rf frequency, the velocity is typically less than 1.1 mm/rf cycle between succeeding wall impacts *to the same direction as the wave propagates*, i.e., away from the source. In this aspect, the multipacting electrons behave differently from the typical field emission electrons that tend to move toward the source. Numerical calculations suggest that the distance between successive wall impacts is roughly of the form¹²

$$\sim \frac{fd^2}{1+n}. \quad (25)$$

More generally, we may consider superposition of the SW and TW fields, i.e., a mixed wave case. The mixed waves can be expressed as follows:

$$\begin{aligned} \mathbf{E}(r, z, \varphi) &= \Re \left(\frac{U}{2r \ln(b/a)} \left(e^{-i(\varphi-kz)} - R' e^{-i(\varphi+kz)} \right) \right) \mathbf{e}_r, \\ \mathbf{B}(r, z, \varphi) &= \Re \left(\frac{U}{2cr \ln(b/a)} \left(e^{-i(\varphi-kz)} + R' e^{-i(\varphi+kz)} \right) \right) \mathbf{e}_\theta, \end{aligned} \quad (26)$$

where R' , $|R'| \leq 1$, is a complex number. Writing R' in polar coordinates $R' = Re^{i\psi}$, $0 \leq R \leq 1$, the fields allow a representation

$$\mathbf{E} = RE_{\text{SW}} + (1 - R)E_{\text{TW}}, \quad \mathbf{B} = RB_{\text{SW}} + (1 - R)B_{\text{TW}}, \quad (27)$$

where z and φ are shifted appropriately. In the straight coaxial line this shifting can be ignored. A computation of the counter functions with different values of the reflection coefficient R shows an interesting feature. When the reflection coefficient is increasing from the initial value $R = 0$, the TW multipacting bands start to split into two different bands. As R is increased to its maximum value $R = 1$ of total reflection, half of these bands coincide with the purely electric multipacting bands of the corresponding order of the SW operation discussed before. Hence, we may recognize multipacting bands in the mixed operation that are electric in nature. The other half of the TW bands shift very quickly to very high incident power region as R increases. An analysis of the stable electron trajectories shows that these levels are due to the *magnetic field*. More specifically, the stable trajectories are found near the maximum of the SW magnetic field, the attracting phase being close to a multiple of π .

Figure 14 displays the gray scale plot of the counter function e_n as a function of the incident power and reflection coefficient. At the bottom of the figure, we have the TW operation ($R = 0$), and at the top the pure SW operation ($R = 1$). The orders of different multipacting processes are indicated in the picture. Furthermore, Figure 14 suggests that the electric multipacting bands due to the higher order processes (order greater than one) disappear when the wave is partially reflected. These bands seem to appear only when the wave form is close to the SW or TW. However, this phenomenon is a graphical artefact, only due to the finite discretization. The electric processes turn out to be repelling in the axial direction. Therefore, the scan of the multipacting power levels must be performed with a very dense grid in the axial direction in order to recognize all possible multipacting processes. The grid used here has been too coarse. Using a finer grid we are able to locate the missing processes.

To summarize the situation we note that in the pure TW operation the multipacting bands are of mixed nature and the electric and magnetic multipacting processes have merged together. As the reflection

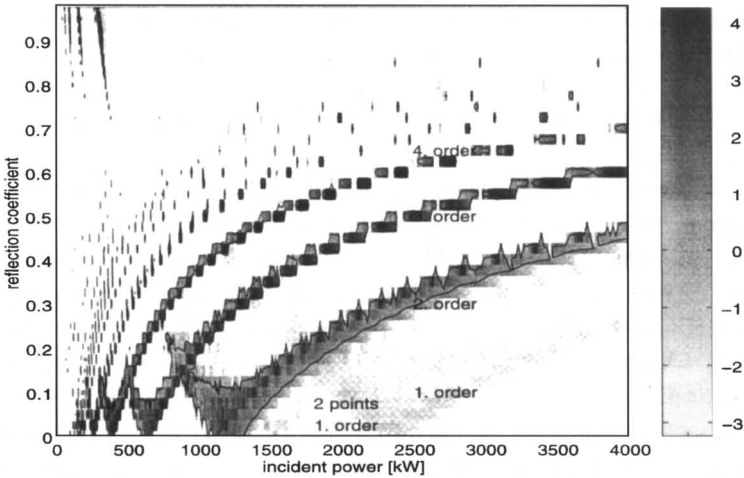


FIGURE 14 The gray scale plot of the 10 base logarithmic of the enhanced counter function e_{30} as a function of the incident power (horizontal axis) in kW and reflection coefficient (vertical axis). In the figure, all positive values of the counter function correspond to the multipacting processes of different order and type. This zero line is indicated in the plot. The outer diameter of the line is 103 mm, frequency is 500 MHz and the impedance is 50.

coefficient increases, the processes of different nature split into electric and magnetic processes. The dependence of the electric multipacting powers on the reflection coefficient can be described approximately by the formula

$$P_R^{\text{electric}} \sim \frac{1}{(1+R)^2} P_{\text{TW}} = \frac{4}{(1+R)^2} P_{\text{SW}}. \quad (28)$$

A heuristic physical explanation for this rule is similar as for the rule relating the SW and TW operations: For given R , the peak voltage is $(1+R)$ times the corresponding peak voltage of the traveling waves. However, the behavior of the magnetic multipacting bands are different. As R increases, the multipacting power levels increase very rapidly. A logarithmic scale plot shows that the increase is faster than polynomial with respect to R .

A closer analysis of electron trajectories shows an important feature. Multipacting in the mixed wave operation is due to certain *fixed points* in the phase space. There seem to be certain locations where the

opposite drifting forces due the SW and TW parts of the magnetic field compensate each other and allow stationary trajectories. These locations, i.e., fixed points, shift in the phase space as the reflection coefficient varies. But, on the other hand, the fixed points are always rather close either to the maximum of the SW electric field (electric multipacting) or to the maximum of the SW magnetic field (magnetic multipacting). Thus, the multipacting electrons do not travel along with the wave when the wave is partially reflected. However, when R is very small, there is a certain limit after which the traveling part of the wave is dominant and the electrons start to travel. This limit seems to be lower for the magnetic processes ($R < 0.05$) than for the electric processes ($R \sim 0.15$).¹²

Furthermore, in the case of the electric multipacting the fixed points are found to be *repelling in the spatial direction but attractive in the phase direction*. In other words, all electrons outside the fixed point in the spatial direction are slowly drifting towards the shadow set. In the previous section the (electric) multipacting in the SW operation was found to behave similarly. However, the magnetic processes behave differently. They are *attractive in both directions*. In other words, electron trajectories starting from a certain phase space neighborhood of the fixed point drift toward the fixed point. Therefore, the magnetic processes are not so sensitive to the perturbations of the field than the corresponding processes of the electric nature. A heuristic explanation to this phenomenon is rather obvious. The TW part of the field drives electrons to one direction only. Therefore, at the maximum of the SW electric field the repelling force due to the SW magnetic field, gives rise to a repelling fixed point in the axial direction. On the other hand, close to the maximum of the SW magnetic field, the SW and TW parts of the field drive electrons to opposite directions, giving arise to an attractive fixed point.

Finally, the scaling laws (21) are found to be valid also for the TW and mixed wave operations, for both the electric and magnetic processes.

3.4 Tapered Lines and Impedance Steps

For the tapered line and the line with an impedance step, any exact analytic formulae for the electromagnetic fields are not available, and we have to resort to a numerical scheme. A short description of the

numerical algorithm used in computing the field map is given in the Appendix. For the trajectory calculations the fields have been computed beforehand in a dense grid and a linear interpolation is used to compute the fields elsewhere.

First consider a $50\ \Omega$ tapered line in the 1300 MHz SW operation. The tapered line is modelled as a closed line with perfectly reflecting ends such that 1300 MHz is a resonant frequency for the resulting closed cavity. The dimensions of the line are indicated in Figure 15.

We choose the length of the line so that the maximum of the electric field is in the tapered area, and so we expect to see multipacting in the tapering. The initial electrons are sent from the whole length of the tapered region with different initial phases.

The overall distribution of the multipacting bands have certain similarity to that computed for a $50\ \Omega$ straight coaxial line in the

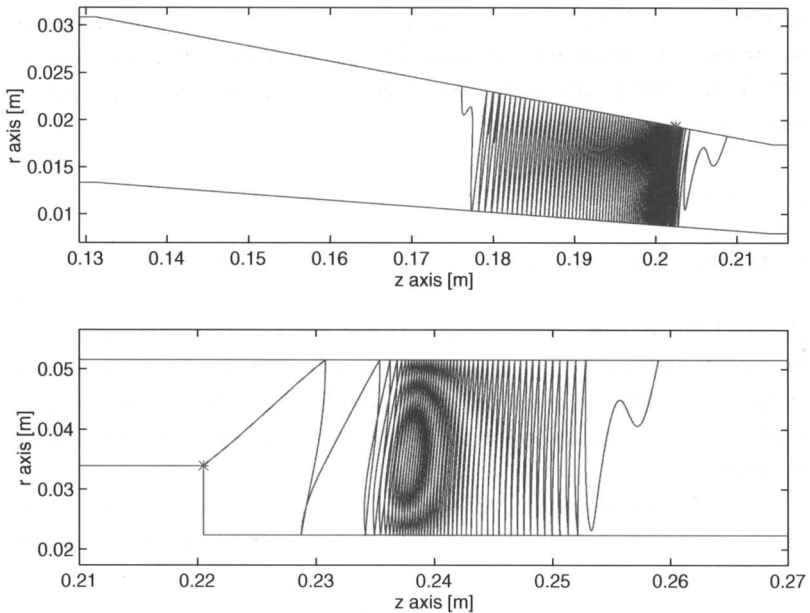


FIGURE 15 Examples of long living trajectories in a tapered line and in a line with an impedance step, causing elevated counter function values. Initial points are marked by asterisks. In the tapered line, the wavelength is $\lambda = 0.2306$ m and the maximum of the electric field lies at $z = 0.175$ m. In the line with the impedance step, the corresponding figures are $\lambda = 0.8517$ m and $z = 0.2$ m.

SW operation. The processes do not appear at the maximum of the electric field. An analysis shows that the most stable trajectories appear where the axial component of the electric field and the axial component of the force $\mathbf{v} \times \mathbf{B}$ due to the magnetic field compensate each other to allow stationary trajectories. Figure 15 shows two relatively long-living electron trajectories in a tapered line. It seems that the trajectories in the tapering are not as stable as those in a straight coaxial line. This suggests that tapering might be used to reduce multipacting.

The second geometry is a coaxial line with an impedance step, i.e., the radius of the inner conductor has a step, changing the impedance from 25 to 50 Ω . The dimensions are again indicated in Figure 15. The maximum of the electric field is close to the impedance discontinuity. A multipacting analysis shows that when the maximum is on the side of lower impedance, stable trajectories appear on the side of the higher impedance. Again, the stable trajectories appear where the axial component of the electric field due to the step compensates the axial force due to the magnetic field. A long-living trajectory initiating from the corner of the step is depicted in Figure 15.

4 METHODS TO SUPPRESS MULTIPACTING

The present work is aimed mainly to develop and to demonstrate the general ideas how to find multipacting levels. In forthcoming works, these ideas will be applied to analyze different methods to suppress multipacting and to analyze multipacting in more specific geometries, including windows, etc. In the suppressing methods we have so far studied the effect of grooving to multipacting as well as DC biasing, static magnetic perturbations and perturbations of the frequency of the rf field. Our preliminary results show that with our multipacting analysis method, it is possible to optimize the perturbations of the cavity geometry or the fields, so that we can suppress the multipacting to acceptably low levels. To demonstrate the power of our method, we consider here a DC biasing voltage in a coaxial line.

4.1 DC Bias

Consider the standing wave operation in a straight coaxial line perturbed with a DC biasing voltage between the conductors, i.e.,

$$\mathbf{E}(x, \varphi) = \mathbf{E}_{\text{sw}}(x, \varphi) + \frac{V}{r \ln(b/a)} \mathbf{e}_r, \quad (29)$$

where V is a constant biasing voltage. By a DC voltage we try to generate a repelling force in order to break the multipacting conditions (1) and/or (2). In the numerical experiments we use both the negative and positive voltages and for each value of V , the multipacting levels are computed and identified. We have restricted the scan to the electric field maximum. Figure 16 displays the gray scale plot of the base 10 logarithm of the relative enhanced counter function e_n as a function of the incident power and biasing voltage. The orders of different multipacting processes are indicated in the picture.

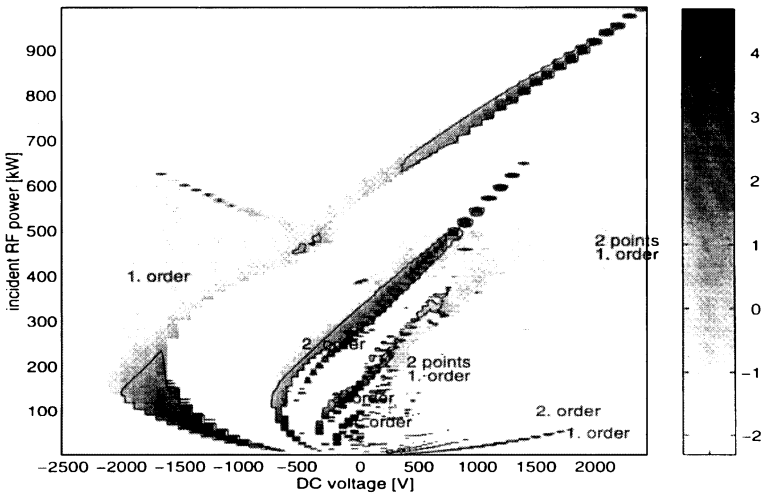


FIGURE 16 The gray scale plot of the base 10 logarithm of the relative enhanced counter function e_n , after 30 impacts, as a function of the incident power (vertical axis) in kW and biasing voltage (horizontal axis) in V. Note that when multipacting occurs, the logarithm of the relative enhanced function is positive, i.e., the number of the electrons is increased. This zero-line is indicated in the plot. The computations correspond to the 500 MHz, 50 Ω coaxial line with the outer diameter of 103 mm.

The plot suggests that by coupling the DC bias to the rf voltage one can raise the rf field from zero to the desired value without crossing any multipacting bands. The scheme should be such that the ramping path in Figure 16 does not cross any of the bands. One simple possibility, for instance, is to use a fixed biasing voltage of -2100 V. Then the first order one-point process starts around 150 kW, but the impact energy is too high for the secondary electron yield to generate multipacting. Another promising possibility is to use high positive voltages, higher than 2000 V. Then a process corresponding to a multipacting process appears above 900 kW.

Figure 16 shows two families of one-point processes, the one on the positive voltages (narrow bands near the lower right corner of Figure 16), and the other on the negative voltages (broad bands). The latter family coincides with the processes of corresponding order of the pure SW multipacting, i.e., when $V=0$, and the processes continue to positive voltages, too. A closer analysis of electron trajectories show the different behavior of these processes. The family on the positive side appears on the inner conductor and the family on the negative side appears on the outer conductor. Figure 17 shows the trajectories.

A further analysis of varying the dimensions of the line and the frequency of the field shows that the multipacting bands shown in Figure 16 remain the same but they scale according to the following rules. The y -axis of the figure, i.e., the incident rf power obeys the previously found scaling laws (21) and the x -axis of the figure, i.e., the biasing voltage scales like

$$V_{\text{one-point}} \sim (fd)^2 Z, \quad V_{\text{two-point}} \sim (fd)^2 Z^2, \quad (30)$$

where f is the frequency, d is the outer diameter, Z is the impedance of the line and V is the biasing voltage. Thus, the above scaling laws together with the scaling laws for the incident power (21), can be used to determine multipacting bands of Figure 16 for any coaxial line with the SW operation. Furthermore, when the wave switches from the standing wave to the traveling wave, the dependence of the multipacting bands of Figure 16 on the reflection coefficient can be described by our previously found formula (28). Of course, when the wave is partially reflected this gives an incomplete picture, since there are also processes which are of magnetic nature. The magnetic multipacting

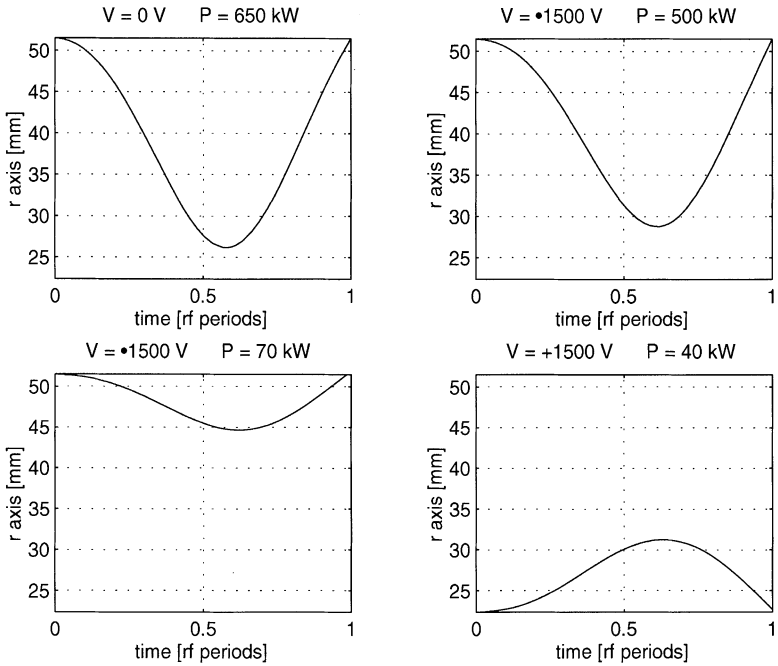


FIGURE 17 Electron trajectories in radius/time scale due to the one-point process of order one. The first picture on the top-left shows the trajectory without the DC bias. The pictures on the top-right and bottom-left give the trajectories when DC voltage is -1500 V and the rf power is 500 kW (top) and 70 kW (bottom). Finally the last picture shows the trajectory when the DC voltage is $+1500$ V and the rf power is 40 kW. In all pictures the upper and lower borders of the pictures correspond to the outer and inner conductors of the line and the electrons are initiated from the maximum of the electric field. The computations correspond to the 500 MHz, 50Ω coaxial line with the outer diameter of 103 mm.

power levels shift again very rapidly to very high power regions and, especially, a magnetic process appears always on a higher power level than the corresponding electric process. For more details we refer to literature.¹³

5 SUMMARY AND CONCLUSIONS

In this article, we describe a systematic computational way to analyze electron multipacting in rf structures. We are able to recognize those rf power levels that are able to multipact and thereafter, to locate and identify the possible multipacting processes. The basis of the analysis

consists of standard trajectory calculations in relativistic dynamics. The novel feature here is to analyze the general nearly periodic structures of the resonant trajectories by using a special distance function defined in a multidimensional phase space and other ideas arising from the theory of dynamical systems.

The approach is applied numerically to analyze multipacting in coaxial structures for standing, traveling and mixed wave operations. For straight coaxial lines, our algorithm enables us to find simple scaling laws for the multipacting power bands with respect to the dimensions, frequency and impedance of the line. By these laws, one can shift the multipacting bands by altering the design of the line in an appropriate way. Furthermore, we studied the effect of DC biasing to multipacting. With our present multipacting analysis method, it is possible to optimize the perturbations and suppress the multipacting to acceptably low levels.

The concepts arising from the theory of dynamical systems provide effective tools for analyzing the multipacting phenomenon. The numerical methods developed here can be used to analyze multipacting in any geometry, including structures with dielectric windows. The use of the general theory developed for dynamical systems³ is still limited in this work, and we believe that the analysis can be developed much further by using, e.g., probability densities in connection with superconducting structures. Especially important issues are to find effective measures for the stability of the various multipacting processes as well as methods for estimating the multipacting currents. From the physical point of view, this would require more detailed analysis of the dynamical onset of the processes as well as their coupling to the field itself.

References

- [1] U. Klein and D. Proch: Multipacting in superconducting RF structures. Talk presented at the *Conference on Future Possibilities for Electron Accelerators*, Charlottesville, 1979. WU B 78-34.
- [2] L.P. Landau and E.M. Lifshitz: *Course of Theoretical Physics*, Vol. 2. Pergamon, 1976.
- [3] A. Lasota and M.C. Mackey: *Chaos, Fractals and Noise*. Springer Verlag Applied Mathematical Sciences 97, New York, 1994.
- [4] C.M. Lyneis, H.A. Swettman and J.P. Turneaure: Elimination of electron multipacting in superconducting structures for electron accelerators. *Appl. Phys. Lett.* **31** (1977), 541–543.
- [5] H. Piel: Superconducting cavities. In: *Proceedings of the CERN Accelerator School: Superconductivity in Particle Accelerators*, Geneva, 1989, pp. 149–196.

- [6] D. Proch, D. Einfeld, R. Onken and N. Steinhauser: Measurement of multipacting currents of metal surfaces in RF fields. WPQ24, *IEEE Proceedings, PAC 95*, pp. 1776–1778.
- [7] E. Somersalo, P. Ylä-Oijala and D. Proch: Electron multipacting in RF structures. TESLA Reports 14-94.
- [8] E. Somersalo, P. Ylä-Oijala and D. Proch: Analysis of multipacting in coaxial lines. FAE08, *IEEE Proceedings, PAC 95*, pp. 1500–1502.
- [9] J. Tuckmantel: One point multipacting levels determined without electron tracking. In: *European Organization for Nuclear Research Series Notes*, 1 August 1989, pp. 569–579.
- [10] R. Woo: Multipacting discharges between coaxial electrodes. *J. Appl. Phys.* **39** (1968) 1528–1533.
- [11] A. Woode and J. Petit: Investigations into multipactor breakdown in satellite microwave payloads. *ESA Journal*, **14** (1990) 467–477.
- [12] P. Ylä-Oijala: Analysis of electron multipacting in coaxial lines with traveling and mixed waves. TESLA Reports 97-20.
- [13] P. Ylä-Oijala: Suppressing electron multipacting in coaxial lines by DC voltage. TESLA Reports 97-21.

APPENDIX: FIELD COMPUTATION

In this appendix, we give a brief summary of the field computation algorithm used to produce the field maps when no analytical solutions are available. The method is based on the boundary integral equation approach for solving Maxwell's equations. Since multipacting is a possibly unstable phenomenon with respect to perturbations in the rf fields, special emphasis has been put on the accuracy of the computation near the cavity walls.

We assume that the cavity as well as the fields are axisymmetric, and consider the TM-mode. The current version is capable of modelling an open resonator having both electric and magnetic ends, and of modelling a segment of a coaxial line with a ceramic dielectric window. The dielectric case is not discussed here.

We represent the electric and magnetic field in terms of the electric and magnetic surface currents, $\mathbf{J} = -\mathbf{n} \times \mathbf{H}$ and $\mathbf{M} = -\mathbf{n} \times \mathbf{E}$, respectively. Here \mathbf{n} stands for the exterior unit normal vector of a surface. Our harmonic time factor is $e^{-i\omega t}$. Denoting by $\partial\Omega$ the boundary of the cavity Ω , we have the equations

$$\mathbf{E}(x) = -\frac{1}{i\omega\epsilon} (\nabla \times)^2 \mathcal{S}_\Omega(\mathbf{J})(x) + \nabla \times \mathcal{S}_\Omega(\mathbf{M})(x), \quad (31)$$

$$\mathbf{H}(x) = \nabla \times \mathcal{S}_\Omega(\mathbf{J})(x) + \frac{1}{i\omega\mu} (\nabla \times)^2 \mathcal{S}_\Omega(\mathbf{M})(x), \quad (32)$$

where the integral operator S_Ω is

$$S_\Omega(\mathbf{I})(x) = \int_{\partial\Omega} \Phi(k, x-y)\mathbf{I}(y) dS(y), \quad x \in \Omega, \quad (33)$$

with

$$\Phi(k, x-y) = \frac{e^{ik|x-y|}}{4\pi|x-y|}, \quad k = \omega\sqrt{\mu\varepsilon}. \quad (34)$$

For the $\text{TM}_{0,n,p}$ -mode, we may write the electric and magnetic currents as

$$\mathbf{J}(x) = j_r(r, z)\mathbf{e}_r + j_z(r, z)\mathbf{e}_z, \quad \mathbf{M}(x) = m_\theta(r, z)\mathbf{e}_\theta.$$

Since in the $\text{TM}_{0,n,p}$ -mode the magnetic current has only the angular component which is independent of the angular variable, the surface divergence of \mathbf{M} vanishes, that is $\text{Div } \mathbf{M} = 0$. By writing $(\nabla \times)^2 = \nabla \nabla \cdot - \Delta$, using the continuity of the electric current and the fact that S is the solution of the Helmholtz equation, Eqs. (31) and (32) may be written by integration by parts as

$$\mathbf{E}(x) = -\frac{1}{i\omega\varepsilon} (\nabla S_\Omega(\text{Div } \mathbf{J})(x) + k^2 S_\Omega(\mathbf{J})(x)) + \nabla \times S_\Omega(\mathbf{M})(x), \quad (35)$$

$$\mathbf{H}(x) = \nabla \times S_\Omega(\mathbf{J})(x) - i\omega\varepsilon S_\Omega(\mathbf{M})(x), \quad (36)$$

$x \in \Omega.$

The geometries considered in Section 3.4 are modelled as closed lines with perfectly reflecting ends at the resonance distances. Therefore, they require the solutions with electric type boundary conditions,

$$\mathbf{n} \times \mathbf{E} = 0, \quad (37)$$

only. If the point $x \in \Omega$ approaches the boundary $\partial\Omega$, then the layer potentials S_Ω , $K_\Omega = \nabla \times S_\Omega$ and $D_\Omega = (\nabla \times)^2 S_\Omega$ have the well-known limiting behavior

$$\lim_{x \rightarrow \partial\Omega} S_\Omega(\mathbf{I}) = S(\mathbf{I}), \quad (38)$$

$$\lim_{x \rightarrow \partial\Omega} K_\Omega(\mathbf{I}) = K(\mathbf{I}) + \frac{1}{2} \mathbf{n} \times \mathbf{I}, \quad (39)$$

$$\lim_{x \rightarrow \partial\Omega} D_\Omega(\mathbf{I}) = D(\mathbf{I}) + \frac{1}{2} \mathbf{n} \text{Div } \mathbf{I}, \quad (40)$$

where S is the single layer potential operator, i.e., the integral (33) with $x \in \partial\Omega$. The integral operators K and D are defined as principal value integrals by the formulae

$$K(\mathbf{I})(x) = \int_{\partial\Omega} \nabla_x \Phi(k, x - y) \times \mathbf{I}(y) \, dS(y), \quad (41)$$

$$D(\mathbf{I})(x) = \int_{\partial\Omega} \nabla_x \Phi(k, x - y) \text{Div} \mathbf{I}(y) \, dS(y) + k^2 \int_{\partial\Omega} \Phi(k, x - y) \mathbf{I}(y) \, dS(y). \quad (42)$$

Since there is no magnetic current present on the perfectly conducting wall ($\mathbf{n} \times \mathbf{E} = 0$), the electric boundary condition (37) yields, with the boundary behavior of the layer potential D_Ω (40), an integral equation

$$-\frac{1}{i\omega\epsilon_0} \mathbf{n}(x) \times \nabla S(\text{Div} \mathbf{J})(x) + i\omega\mu_0 \mathbf{n}(x) \times S(\mathbf{J})(x) = 0, \quad (43)$$

with $x \in \partial\Omega$.

Equation (43) is discretized by approximating the current in an appropriate basis and using the Ritz–Galerkin method. We write the approximation for the electric current as

$$\mathbf{J}(x) = \sum_{l=1}^N \alpha_l \mathbf{j}_l(x). \quad (44)$$

In the present application, a piecewise linear approximation is used.

We multiply Eq. (43) by $i\omega\epsilon_0 \mathbf{n} \times \mathbf{j}_k$, $k = 1, \dots, N$, and integrate over the surface $\Gamma = \partial\Omega$. We obtain the equations

$$\begin{aligned} & \int_{\Gamma} \text{Div} \mathbf{j}_k(x) S(\text{Div} \mathbf{J})(x) \, dS(x) \\ & - k^2 \int_{\Gamma} \mathbf{j}_k(x) \cdot S(\mathbf{J})(x) \, dS(x) = 0, \quad k = 1, \dots, N. \end{aligned} \quad (45)$$

A substitution of the approximation (44) of the electric current to the integral equation above, yields to a homogeneous matrix equation of the type

$$Ac = 0. \quad (46)$$

Here c is a vector containing the coefficients of the piecewise linear basis functions, i.e., $c = [\alpha_1, \dots, \alpha_N]^T$. Hence, the integral equation method is reduced to the problem of finding a non-zero c satisfying the above matrix equation. Obviously, if A is non-singular, the only solution of the matrix equation is $c = 0$. This property can be used for finding the resonances of a given structure, by studying the condition number of $A(\xi)$, depending on a free parameter ξ . The parameter ξ may be, e.g., the rf frequency or the length of the resonator. When at resonance, the condition number of $A(\xi)$ explodes, and the solution $c \neq 0$ of Eq. (46) is (a constant times) the eigenvector of A corresponding to the least singular value of the matrix A .

Once the coefficients c are solved, the fields \mathbf{E} and \mathbf{H} can be evaluated using the representations (31) and (32). The field computation is designed so that the field values are obtained with high accuracy even at points close to the walls. Details are omitted here.

For the geometries having ceramic windows, the application of boundary integral equations yields not only a single integral equation, but a set of integral equations. The resulting equations can be solved in the similar fashion as above.

More details about the field computations, including ceramic windows, will be presented in a forthcoming paper by the authors.